Tailoring grain boundary structures and chemistry of Ni-rich layered cathodes for enhanced cycle stability of lithium-ion batteries

Pengfei Yan[1,2,5], Jianming Zheng[3,5], Jian Liu[4], Biqiong Wang[4], Xiaopeng Cheng[2], Yuefei Zhang[2], Xueliang Sun[4]*, Chongmin Wang [1]* and Ji-Guang Zhang [3]*

A critical challenge for the commercialization of layer-structured nickel-rich lithium transition metal oxide cathodes for battery applications is their capacity and voltage fading, which originate from the disintegration and lattice phase transition of the cathode particles. The general approach of cathode particle surface modification could partially alleviate the degradation associated with surface processes, but it still fails to resolve this critical barrier. Here, we report that infusing the grain boundaries of cathode secondary particles with a solid electrolyte dramatically enhances the capacity retention and voltage stability of the cathode. We find that the solid electrolyte infused in the boundaries not only acts as a fast channel for lithium-ion transport, it also, more importantly, prevents penetration of the liquid electrolyte into the boundaries, and consequently eliminates the detrimental factors, which include cathode–liquid electrolyte interfacial reactions, intergranular cracking and layered-to-spinel phase transformation. This grain-boundary engineering approach provides design ideas for advanced cathodes for batteries.

The goal of rechargeable lithium-ion batteries is to build a battery with a high energy density, long cycle stability, high rate and safe operation[1,2]. These objectives are achievable either through exploring new battery materials[3,4] or optimizing the existing battery components[5–7]. To facilitate electron and ion transport in electrodes, active particles must be well dispersed to ensure that each particle is in close contact with conducting additives and wetted by liquid electrolytes. However, this design principle intuitively counters against the high-density loading of nanometre-sized electrode particles, and direct contact between the electrode and liquid electrolyte often leads to deleterious side reactions, which consequently limit the battery's attainable capacity density and cycle stability. Therefore, to increase the cathode's packing density, nanometre-sized primary particles are intentionally aggregated to form micrometre-sized secondary particles, which, however, introduces new challenges[8].

It has been observed that on cycling, high-density intergranular cracks typically initiate within secondary particles, which leads to disintegration of the particles, poor cycle stability and eventual battery failure[9]. Further, permeation and penetration of liquid electrolytes along the grain boundaries and cracks in the secondary particles worsen the problems associated with the cathode–liquid reaction[10–12], and the resulting layered cathodes undergo phase transformation, which contributes to voltage fading. Thus, advancements for lithium-ion batteries critically rely on resolving these bottleneck problems[8,13].

Tailoring the grain boundary structure and chemistry for the optimization of material behaviours and properties appears to be a classic protocol in material science[14–17]. However, this strategy has not been systematically studied or applied to electrode

materials for rechargeable lithium-ion batteries. In this work, we infuse a solid electrolyte, Li_3PO_4 (hereafter referred to as LPO), into the grain boundaries of a nickel (Ni)-rich layered cathode material, $LiNi_{0.76}Mn_{0.14}Co_{0.10}O_2$ (hereafter referred to as Ni-rich NMC) to tackle its capacity and voltage decay issues. The process reveals a dramatically enhanced cycling stability of the cathode. Detailed structural and chemical analyses combined with electrochemical testing indicate that a thin layer of the LPO solid electrolyte infused into the grain boundary not only prevents the cracking of the secondary particles and the layered-to-spinel phase transformation, but also improves the cathode–electrolyte interfacial kinetics, which enables an excellent cycle stability of the Ni-rich cathode. This three-dimensional (3D) grain-boundary engineering approach differs from previous ones in which LPO solid electrolytes were used as a 2D coating layer on the particle surface to improve the cycle stability of cathode materials[18–20].

Enhanced capacity retention and voltage stability

The Ni-rich NMC was synthesized via a co-precipitation method, and initially the calcination temperature was optimized carefully to achieve the optimal electrochemical performance (Supplementary Fig. 1). The secondary particles of Ni-rich NMC prepared at the optimal conditions (750 °C) were further coated with LPO using atomic layer deposition (ALD)[6,21]. After the ALD coating, the LPO-coated particles were further annealed at 600 °C for two hours in air to enable the infusion of LPO along the grain boundaries of the secondary particles. To reveal the function of LPO, three types of electrode were fabricated using uncoated, LPO-as-coated and LPO-infused particles of Ni-rich NMC. The electrodes were charged/discharged for 200 cycles within a voltage window of about 2.7–4.5 V

[1]Environmental Molecular Sciences Laboratory, Pacific Northwest National Laboratory, Richland, WA, USA. [2]Institute of Microstructure and Properties of Advanced Materials, Beijing University of Technology, Beijing, China. [3]Energy and Environment Directorate, Pacific Northwest National Laboratory, Richland, WA, USA. [4]Nanomaterials and Energy Lab, Department of Mechanical and Materials Engineering, University of Western Ontario, London, Ontario, Canada. [5]These authors contributed equally to this work: Pengfei Yan, Jianming Zheng. *e-mail: xsun9@uwo.ca; Chongmin.wang@pnnl.gov; Jiguang.zhang@pnnl.gov
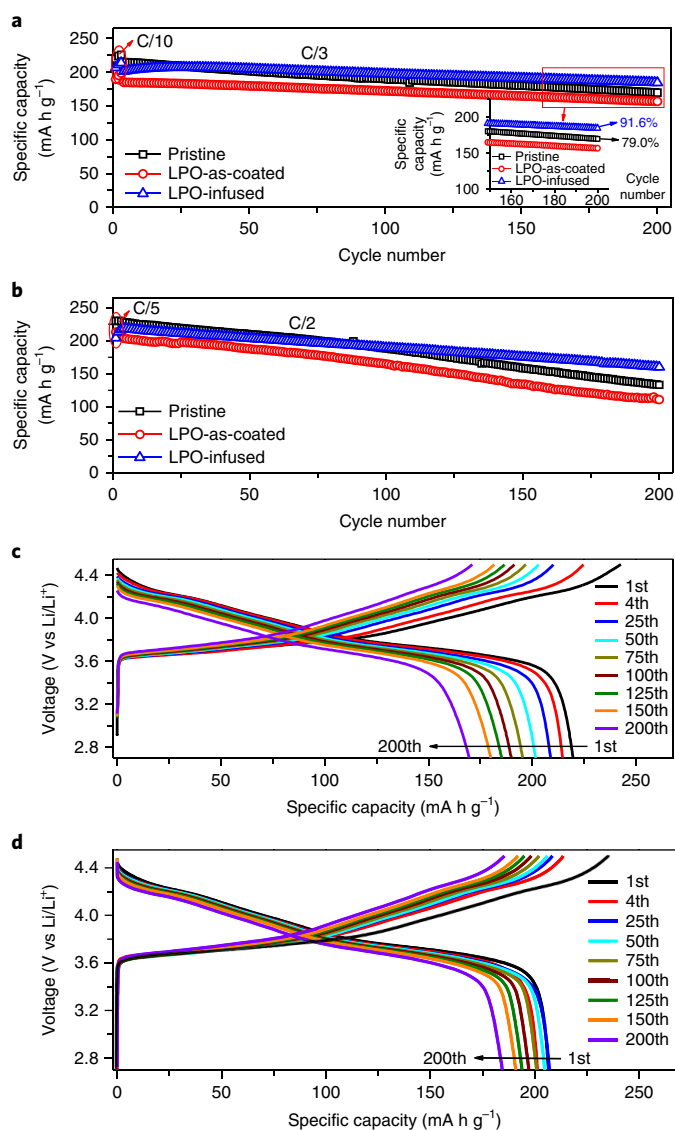
Fig. 1 | Effects of LPO infusion on the electrochemical performance.
a–**d**, Cycling performance of the three Ni-rich NMC cathodes in the voltage range 2.7–4.5 V at room temperature (**a** and **c**) and at 60 °C (**b** and **d**). **a**, Specific capacity retention after 200 cycles. The half-cell is cycled at C/3 after three formation cycles at C/10. Inset: the magnified area (red frame) shows that the capacity retention is 91.6% for the LPO-infused cathode and 79.0% for the pristine cathode. **b**, Specific capacity as a function of cycle numbers when cycled at 60 °C. The half-cell is cycled at C/2 after three formation cycles at C/5. **c**, The charge/discharge voltage profile evolution of the pristine cathode at room temperature. **d**, The charge/discharge voltage profile evolution of the LPO-infused cathode at room temperature.

Fig. 2 | Tracking the spatial distribution of LPO prior to battery cycling.
a,**b**, STEM–HAADF image (**a**) and EDS map of P (**b**) of the as-coated sample, which indicate that the LPO is a layer that covers the surface of the secondary particle. Scale bar, 500 nm. **c**,**d**, STEM image (**c**) and EDS map of P (**d**) of the LPO-infused sample, which indicates infusion of the LPO in the secondary particles. Scale bar, 1 μm. **e**,**f**, High-resolution STEM image (**e**) and EDS map of P (**f**) from the region shown by a red box in **c**, which indicates the penetration of LPO along the grain boundaries in the secondary particles. Scale bar, 20 nm. **g**, The schematic illustration shows the evolution of the LPO coating layer on the secondary particle following coating and annealing.

(described in detail in Methods). The LPO-infused electrode demonstrated the highest capacity retention of 91.6% at room temperature and 73.2% at 60 °C, in contrast to the 79.0% and 58.3%, respectively, for uncoated particles (Fig. 1a,b). On the other hand, the LPO-as-coated electrode exhibited less capacity as compared with the LPO-infused electrode, as shown in Fig. 1a,b. Accompanied with the stable capacity retention was a dramatically reduced voltage decay for the case of the LPO-infused particles, as shown in the charge–discharge voltage profiles (Fig. 1c,d). In terms of rate performance, the LPO-infused electrode showed a comparable rate to that of the uncoated one, whereas the LPO-as-coated electrode showed a
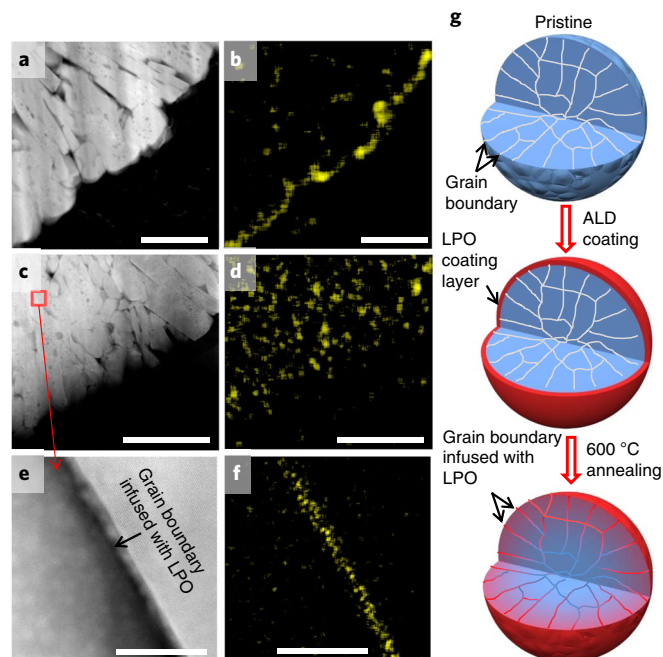
poor rate performance (Supplementary Fig. 2). These observations indicate that applying the LPO coating on the outer surface of the secondary particle has a limited effect on the performance improvement. However, annealing in air at 600 °C for two hours not only led to a superior cycle stability, but also enabled an enhanced rate performance. Similarly, electrochemical performance testing under a full-cell configuration with graphite as the anode also showed an enhanced cycling stability after the infusion of LPO in the Ni-rich NMC (Supplementary Fig. 3).

Infusion of solid electrolyte into the grain boundaries
To understand how the infusion process significantly enhances the cycling stability of the capacity and voltage, we investigated the structural and chemical features of the aforementioned three types of particle in both the fresh and cycled states. First, the spatial distribution of the coating materials before the battery cycling was identified. For the uncycled particles, phosphorus (P) is unique and can be used as a signature element to trace the spatial distribution of the LPO coating layer. Scanning transmission electron microscopy–energy-dispersive X-ray spectroscopy (STEM–EDS) mapping of the P distribution indicates that, after the ALD coating, LPO was located primarily at the surface of the secondary particle with a coating layer thickness of tens of nanometres, as shown in Fig. 2a,b. After two hours of annealing in air at 600 °C, the P-enriched surface coating layer disappeared, as shown in Fig. 2c,d. Instead, P-enriched regions were found within the secondary particles. High spatial resolution mapping of the P distribution indicates that the grain boundaries and pockets of the triple grain junction were enriched with P (Fig. 2e,f and Supplementary Fig. 4). This demonstrated
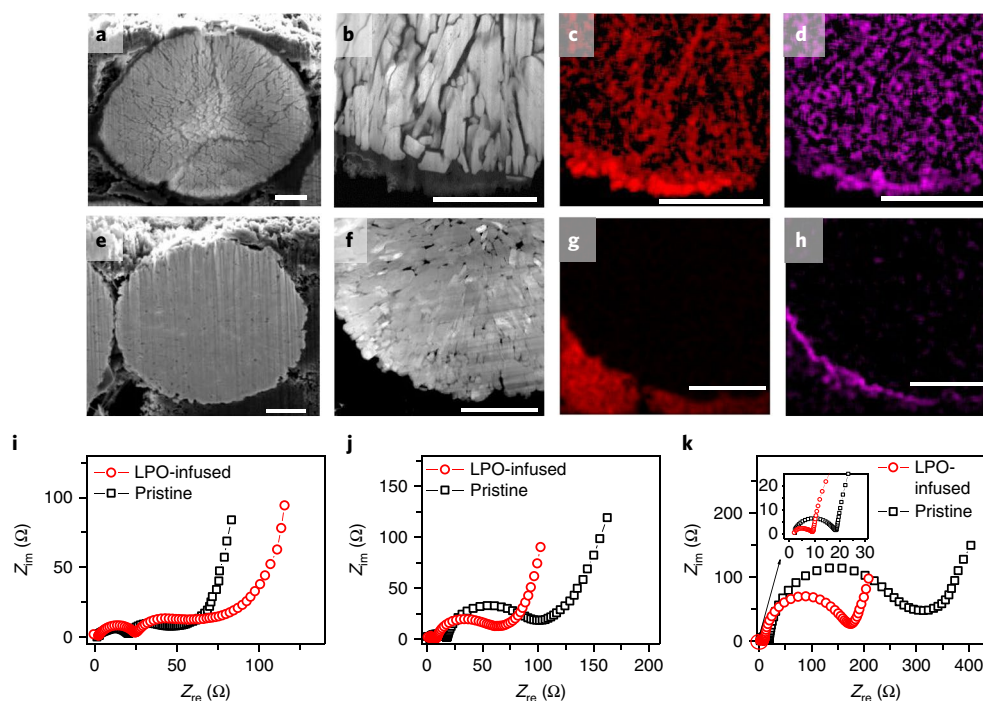
Fig. 3 | Infusion of LPO into secondary particles eliminates intergranular cracking. a–d, Cross-sectional SEM image (**a**), STEM–HAADF image (**b**) and the corresponding C (**c**) and F (**d**) maps (two signature elements from the electrolyte) from the pristine electrode after 200 cycles, indicating the formation of intergranular cracks and penetration of electrolyte along the grain boundaries. **e–h**, Cross-sectional SEM image (**e**), STEM–HAADF image (**f**) and the corresponding C (**g**) and F (**h**) maps from the LPO-infused electrode after 200 cycles, which show no intergranular cracks and the absence of electrolyte-related species along the grain boundaries in the secondary particles. Scale bars, 2 μm. **i–k**, Impedance spectra evolution of the pristine electrode and the LPO-infused electrode at the 1st (**i**), 10th (**j**) and 50th cycles (**k**). im, imaginary; re, real.

that during the 600 °C annealing, the LPO coating layer initially located at the surface of the secondary particle infused into the grain boundaries of the secondary particles, as schematically illustrated in Fig. 2g. High-resolution transmission electron microscopy (TEM) imaging and electron diffraction analysis indicate that, after the ALD coating, the LPO was in an amorphous state (Supplementary Fig. 5). Thus, its melting point should be notably lower than that of crystalline LPO (837 °C), which enables the LPO penetration along the grain boundary of the secondary particle. The coating and subsequent annealing led to a slight increase of cation mixing at the outermost surface layer in the LPO-infused electrode compared with that in the pristine one (Supplementary Fig. 6), which may slightly decrease the lithium-ion diffusion kinetics and partly account for the initial lower capacity and decreased rate performance. However, the ALD coating and subsequent annealing did not modify the general morphology (Supplementary Fig. 7) and structure (Supplementary Fig. 8) of the secondary particles, as evident by scanning electron microscopy (SEM) imaging and powder X-ray diffraction measurements.

Elimination of cracking and related detrimental factors

After 200 cycles, the three particle types showed distinctively different structural features, as demonstrated by the cross-sectional and surface SEM images of the secondary particles (Fig. 3 and Supplementary Figs. 9 and 10). The uncoated particle featured the formation of intensive intergranular cracks (Fig. 3a and Supplementary Figs. 9b and 10a), which have been identified as one of the major structural degradation mechanisms that lead to cathode failure during battery cycling[8,9,22]. Surprisingly, these cracking features did not occur in the LPO-infused samples (Fig. 3e and Supplementary Figs. 9d and 10b). Apparently, the infusion of LPO

into the grain boundaries of the secondary particles prevented the formation of intergranular cracking in the secondary particles and, correspondingly, the associated degradation route.

Consistent with the structural differences described above are the chemical differences among these three samples after 200 cycles, which reflect a distinctively different interaction of the liquid electrolyte with the cathode after the LPO coating and infusion into the grain boundaries. Fluorine (F) and carbon (C) are components of the liquid electrolyte, but they are not part of the cathode particles. Therefore, the spatial distribution of F and C can be used to trace the interaction of the electrolyte and the cathode particles. As shown in Fig. 3b–d, for the uncoated particles, both F and C showed enrichment within the cycled secondary particles. This means that the liquid electrolyte penetrated along the grain boundaries of the uncoated secondary particles. The side reaction between the cathode and liquid electrolyte led to the formation of species such as Li_2CO_3, LiF and $LiFPO_x$ (refs [10,12]), as supported by the EDS and electron energy-loss spectroscopy (EELS) analyses shown in Supplementary Fig. 11. Apparently, the formation of these species led to electrolyte consumption, salt depletion in the electrolyte and the formation of a thick solid electrolyte interphase (SEI) layer on the surface and along the grain boundary of the cathode particles. These SEI layers modified the cathode–electrolyte interfacial electrochemistry and are detrimental to battery stability. Surprisingly, for the LPO-infused particles after battery cycling, C and F only appeared at the outer surface of the secondary particles, not within them (Fig. 3f–h), which indicates that during battery cycling the liquid electrolyte did not penetrate into the grain boundaries of the secondary particles. Thus, no interfacial side-reaction products were observed within the secondary particles. As a direct result for the LPO-infused electrode, the cathode–electrolyte side reactions

occurred only at the outer surface of the secondary particles, not on the primary particles within them. Specific surface area measurements also confirmed that the LPO-infused sample had a much smaller specific surface area because the intergranular gaps were filled by the LPO. As shown in Supplementary Fig. 12, the specific surface area was $0.3\,m^2\,g^{-1}$ for the LPO-infused sample, which contrasts with $1.0\,m^2\,g^{-1}$ in the pristine one. The structural and chemical differences among the three types of particle described are also corroborated by the electrochemical impedance spectroscopy (EIS) measurement. Attributed to the poor ionic/electronic conductivity induced by the particle cracking and solid–liquid side reaction, the EIS showed that the charge-transfer resistance across the electrode–electrolyte interface increased much faster for the electrode made of uncoated particles compared with that made of LPO-infused particles (the semicircle curves at high to medium frequency in Fig. 3i–k).

Electron diffraction and high-resolution structural imaging revealed more details about how the LPO infusion along the grain boundaries of the secondary particles enhanced the battery cycling stability. Liquid electrolyte was blocked from penetrating into the grain boundaries within the secondary particles by the infused LPO, which eliminated the phase transformation from the original layered structure to spinel/rock salt phases, which otherwise would initiate from the particle surface and propagate inward with the progression of the battery cycling. This point is clearly revealed by the images shown in Fig. 4. For comparison, the microstructural features of the uncoated particle without cycling are shown in Fig. 4a,d,g,j, which reveals dense packing of the layered primary particles within the secondary particle. For the uncoated particle after 200 cycles, shown in Fig. 4b,e,h,k, significant structural evolution is identified. The selected area electron diffraction (SAED) pattern features halo rings with an intensity fluctuation (Fig. 4b), which indicates poor crystallinity due to a severe lattice distortion and defect generation. The bright-field TEM image clearly shows that the boundaries between primary particles become large and are filled with side-reaction products (compare Fig. 4d with Fig. 4e). As a consequence of the solid–liquid reaction, the primary particle surface is also covered with a thin surface layer, marked by the arrows in Fig. 4h. At the atomic level, the layered structure transforms into a rock-salt-like structure (compare Fig. 4j with Fig. 4k). In sharp contrast, the structural evolutions already described for the uncoated particle do not occur for the LPO-infused particles, even after 200 cycles, as revealed in Fig. 4c,f,i,l. This result is further supported by additional STEM–HAADF lattice images with respect to the cation mixing for pristine and LPO-infused materials after 200 cycles (Supplementary Fig. 13).

The LPO-infused cathode material not only showed a good capacity and voltage stability, it also demonstrated an enhanced thermal stability. Increasing the Ni content usually leads to poor thermal stability, which is a critical issue related to safety concerns as demonstrated when in situ X-ray diffraction measurements were made[23]. We found that the LPO-infused cathode showed an improved thermal stability as evidenced by a differential scanning calorimetry (DSC) test (Supplementary Fig. 14). The thermal-decomposition-induced exothermic reaction was considerably suppressed after the LPO infusion—the exothermic peak shifted from 249.2 °C to 261.4 °C and the heat released also decreased from $1,582\,J\,g^{-1}$ to $916\,J\,g^{-1}$.

Mechanism of enhanced cycling stability

Based on our microanalysis, the fundamental mechanisms as to why the LPO-infused electrode exhibited a superior electrochemical performance over the other two electrodes become clear. First, the active cathode material inside the secondary particle is well preserved during the cycling of the LPO-infused electrode. Even after 200 cycles, the interior region shows no noticeable change.
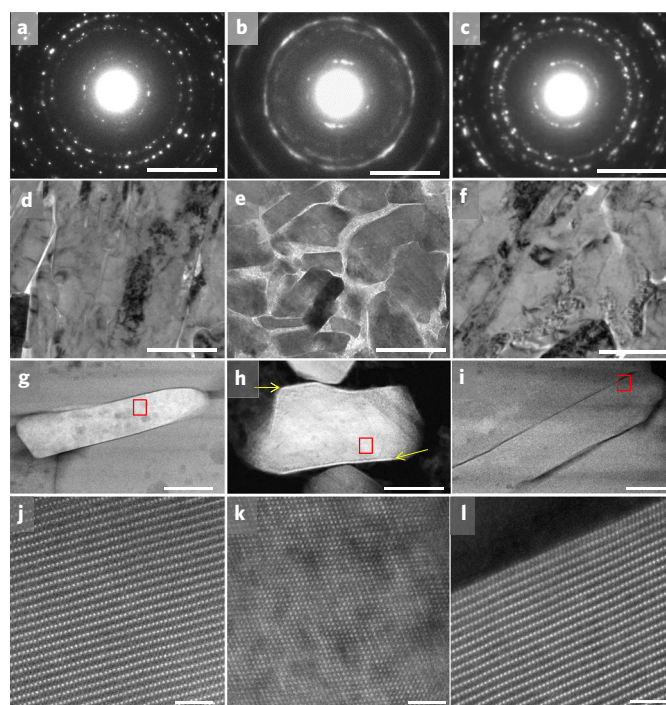

Fig. 4 | Infusion of LPO into secondary particles eliminates structural degradation. a–l, The structural degradations are evaluated by a combination of SAED (**a–c**), bright-field TEM imaging (**d–f**), STEM–HAADF imaging (**g–i**) and atomic-level STEM–HAADF imaging (**j–l**) (which correspond to the high magnification image of the regions in **g–i** marked by red boxes). The left column corresponds to the pristine electrode without cycling, the middle column is the pristine electrode after 200 cycles and the right column shows the LPO-infused electrode after 200 cycles. These observations demonstrate that, after 200 cycles, the pristine electrode shows a significant structural degradation, which features intergranular cracking and the formation of an amorphous phase within the grain boundaries (**e**), the formation of a surface reaction layer on each grain surface (indicated in **h** by the yellow arrows) and a layered-to-spinel transformation (**k**), whereas these degradation features do not occur in the LPO-infused electrode. Scale bars, $5\,nm^{-1}$ (**a–c**), 500 nm (**d–f**), 100 nm (**g–i**), 2 nm (**j–l**).

Second, the annealing process redistributes the surface-coated LPO layer along the grain boundary of the whole secondary particle and enables the fast lithium-ion transport across the cathode without any side reaction with the liquid electrolyte, as evidenced by the first-cycle EIS shown in Supplementary Fig. 15. Third, infusion of LPO solid-state electrolyte into the intergranular boundaries enhances the lithium-ion transfer, and thus improves the rate capability. In addition, the alleviation of the cathode–electrolyte reaction leads to a minimization of the electrolyte decomposition, which also minimizes the electrolyte degradation during cycling. Apparently, the outer surface of the secondary particle remains in contact with the liquid electrolyte, which contributes to the cathode degradation. In principle, a larger secondary particle size leads to a smaller surface-related degradation. Coupled with the additional dedicated surface modifications of the secondary particle to mitigate surface degradation, a more pronounced improvement on battery performance can be expected.

The solid electrolyte infusion into the grain boundaries means solid–solid interfaces form within the secondary particles, which behave as in a solid-state battery. As revealed in Fig. 4f–l, no surface phase transformation occurs at these solid–solid interfaces

after prolonged cycling, which indicates that solid–solid interfaces are more stable than the cathode–liquid interfaces. Moreover, this shows that the direct contact of liquid electrolyte with the layered cathode plays a key role in initiating the widely documented layered-to-spinel transformation at the cathode surface. In terms of the factors that contribute to intergranular cracking, it is believed that the anisotropic lattice expansion and contraction during the charge–discharge cycle causes substantial microstrain among the primary particles and correspondingly leads to the intergranular cracks[22,24–26]. In this work, the LPO-infused cathode has a comparable delithiation level to the uncoated sample. Thus, a similar magnitude of lattice strain should be expected for both samples. The absence of intergranular cracking in the LPO-infused particles indicates that intergranular cracks in the uncoated particles observed in this work (as well as commonly noted by others[9,27]) are essentially the consequences of both the penetration of the liquid electrolyte into the grain boundaries, which induce dissolution of the cathode, and the build-up of microstrain within the lattice. This conclusion is supported by four observations. First, the density of the intergranular cracks is very high, and the separation gaps between the primary particles become large following battery cycling (Figs. 3a,b and 4e and Supplementary Fig. 9b), which cannot be explained solely by the strain-induced cracking as the volume shrinkage is expected to be less than 2%. Second, the cracks preferentially align along the radius direction, which is probably related to the transport process of the dissolved cations in the liquid on battery cycling. Third, in the cycled LPO-as-coated electrode (without infusion), the intergranular cracks are fewer than those in the uncoated particles, which indicates that the outer surface coating of the secondary particle partially blocks the liquid from penetrating the grain boundaries and consequently alleviates the dissolution process and intergranular cracking (Supplementary Figs. 9 and 16). Fourth, if the crack only stems from strain effects, many cracks would be expected in the first few cycles, whereas we find that high-density cracks gradually develop during prolonged cycles[8,9,13,28].

Conclusions

In summary, we clearly demonstrate that the coating and subsequent infusion of the LPO solid-state electrolyte along the grain boundaries of secondary particles in a Ni-rich NMC layered cathode can significantly enhance its structural and interfacial stability, and lead to the long-term cycle stability of both capacity and voltage. Detailed structural and chemical analysis reveals that the dramatically enhanced performance is associated with grain-boundary modification by the solid-state electrolyte, which provides a fast path for the lithium-ion transport and simultaneously prevents penetration of the liquid electrolyte into the boundary. This eliminates several detrimental factors, including the solid–liquid interfacial reaction, intergranular cracking and layered-to-spinel phase transformation, which critically affects the battery cycle stability of both capacity and voltage. The present work provides insights into how the solid–liquid interfacial reaction can affect the battery performance and offers ideas for the design of advanced battery electrode materials via grain-boundary engineering.

Methods

Material preparation. Spherical Ni-rich $Ni_{0.76}Mn_{0.14}Co_{0.10}(OH)_2$ precursors were prepared by a mixed hydroxide co-precipitation method using a continuously stirred tank reactor (CSTR) under a N_2 atmosphere. Initially, the CSTR (5 l capacity) was filled with 1.5 l of distilled water. Then, an aqueous solution composed of $NiSO_4$, $MnSO_4$ and $CoSO_4$ with a concentration of 2.0 mol l^{-1} was continuously pumped into the CSTR. Meanwhile, a NaOH solution (4.0 mol l^{-1}) precipitation reagent and a NH_4OH solution chelating agent (10 mol l^{-1}) were separately fed into the CSTR. The pH value (11.5), stirring speed (1,000 revolutions per minute) and temperature (50 °C) were carefully controlled during the precipitation process. The precursor was filtered, thoroughly washed with distilled water and dried overnight at 110 °C. Ni-rich NMC cathode materials were prepared by mixing the $Ni_{0.76}Mn_{0.14}Co_{0.10}(OH)_2$ precursor powder with LiOH, followed by

sintering at different temperatures for 20 h in air. To compensate for the evaporation of Li during calcination at high temperatures, 3 mol% excess Li was used.

The deposition of lithium phosphate on NMC powders was performed in a Savannah 100 ALD system (Ultratech/Cambridge Nanotech) using lithium *tert*-butoxide (LiO^{t}Bu) and trimethyl phosphate (TMPO) as precursors. The respective source temperatures for LiO^{t}Bu and TMPO were 180 °C and 75 °C, and the deposition temperature for lithium phosphate was 300 °C. Before deposition, NMC powders were well dispersed in a stainless-steel tray, which was put in the centre of a reaction chamber. During one ALD cycle, LiO^{t}Bu and TMPO were alternatively introduced into the reaction chamber with a pulse time of 2 s, and the pulsing of each precursor was separated by a 15 s purge with N_2. A lithium phosphate layer of ~10 nm in thickness (calculated from its growth rate of ~0.07 nm per cycle) was coated on the NMC powders by repeating the described ALD cycle 150 times. The ALD-coated sample was further annealed at 600 °C for 2 h to obtain the ALD-coated annealed sample.

Electrochemical measurements. Electrochemical performance measurements were conducted in R2032 coin-type cells. The thin electrodes were prepared by casting a slurry that contained 80% of the active material, 10% polyvinylidene fluoride binder (Kureha L#1120), and 10% Super-P onto an Al current collector foil. A typical loading of the electrodes is about 4–5 mg cm^{-2}. After drying, the electrodes were punched into disks with an area of 1.27 cm^2. Electrochemical cells were assembled with the cathodes as prepared, metallic lithium foil as the anode electrode, Cellgard 2500 as the separator and 1 M LiPF$_6$ dissolved in ethyl carbonate and dimethyl carbonate (1:2 in volume) as the electrolyte in an argon-filled glove box (Mbraun) with both oxygen and moisture content controlled below 1 ppm. Charge–discharge experiments were performed galvanostatically between about 2.7 and 4.5 V on an Arbin BT-2000 battery tester at room temperature and 60 °C. The rate capability was evaluated using the same charge rate of C/5 and a gradual ascending in the discharge cycle rate after five initial charge–discharge cycles at a C/10 rate. In this work, a 1C rate corresponds to a current density of 200 mA g^{-1}. EIS measurements were performed using a Solartron 1255B frequency analyser and 1287 electrochemical workstation in a frequency range from 100 kHz to 1 MHz with a perturbation amplitude of ±10 mV. For the full-cell testing, the 2032 coin cells were assembled using graphite as an anode. The cathode loading level was around 4.5 mg cm^{-2}, whereas the anode loading level was 5.0 mg cm^{-2}. The N/P ratio was controlled at 1.2. The graphite electrode density was 1.0 g cm^{-3} and the cathode density was 2.2 g cm^{-3}. The cycling voltage window was about 2.5–4.4 V with two formation cycles at 0.1C before long-term cycling at 1C.

Microstructure characterizations. Focused ion beam (FIB)/SEM imaging and TEM specimen preparation were conducted on an FEI Helios DualBeam FIB operated at 2–30 kV. Thin-section TEM specimens were prepared directly from each electrode foil by a standard lift-out procedure. First, a 1.2-µm-thick Pt layer (200 nm electron-beam deposition followed by a 1 µm ion-beam deposition) was deposited on a region to void the Ga ion-beam damage in the subsequent lift-out and thinning process. After lift out, the specimen was thinned to 200 nm using a 30 kV Ga ion beam. Then, a 2 kV final polishing was performed to remove surface damage until electron transparency at 5 kV SEM imaging. After the 2 kV Ga ion polish, the surface damage layer was believed to be less than 1 nm.

The FIB-prepared lithium transition metal oxide samples were investigated by a FEI Titan80–300 S/TEM microscope at 300 kV. The microscope was equipped with a probe spherical aberration corrector, which enabled sub-ångström imaging using STEM–HAADF detectors. For STEM–HAADF imaging, the inner and outer collection angles of the annular dark-field detector were set at 55 and 220 mrad, respectively. STEM–EDS and STEM–EELS were performed on a probe aberration-corrected JEOL JEM-ARM200CF at 200 kV. The STEM–EELS data were collected in dual-EELS mode to obtain both zero-loss and core-loss spectra. Core-loss EELS were calibrated by the corresponding zero-loss EELS before further analysis using DigitalMicrograph (Version 2.11 (Gatan Inc.)).

References

1. Tarascon, J. M. & Armand, M. Issues and challenges facing rechargeable lithium batteries. *Nature* **414**, 359–367 (2001).
2. Etacheri, V., Marom, R., Elazari, R., Salitra, G. & Aurbach, D. Challenges in the development of advanced Li-ion batteries: a review. *Energy Environ. Sci.* **4**, 3243–3262 (2011).
3. Zhou, Y.-N. et al. Tuning charge–discharge induced unit cell breathing in layer-structured cathode materials for lithium-ion batteries. *Nat. Commun.* **5**, 5381 (2014).
4. Lin, D., Liu, Y. & Cui, Y. Reviving the lithium metal anode for high-energy batteries. *Nat. Nanotech.* **12**, 194–206 (2017).

5. Li, W., Song, B. & Manthiram, A. High-voltage positive electrode materials for lithium-ion batteries. *Chem. Soc. Rev.* **46**, 3006–3059 (2017).

6. Liu, J. & Sun, X. Elegant design of electrode and electrode/electrolyte interface in lithium-ion batteries by atomic layer deposition. *Nanotechnology* **26**, 024001 (2015).

7. Manthiram, A., Knight, J. C., Myung, S. T., Oh, S. M. & Sun, Y. K. Nickel-rich and lithium-rich layered oxide cathodes: progress and perspectives. *Adv. Energy Mater.* **6**, 1501010 (2016).

8. Lee, E.-J. et al. Development of microstrain in aged lithium transition metal oxides. *Nano Lett.* **14**, 4873–4880 (2014).

9. Liu, H. et al. Intergranular cracking as a major cause of long-term capacity fading of layered cathodes. *Nano Lett.* **17**, 3452–3457 (2017).

10. Wang, Y. et al. Ti-substituted tunnel-type $Na_{0.44}MnO_2$ oxide as a negative electrode for aqueous sodium-ion batteries. *Nat. Commun.* **6**, 6401 (2015).

11. Edström, K., Gustafsson, T. & Thomas, J. O. The cathode–electrolyte interface in the Li-ion battery. *Electrochim. Acta* **50**, 397–403 (2004).

12. Cresce, A. V., Russell, S. M., Baker, D. R., Gaskell, K. J. & Xu, K. In situ and quantitative characterization of solid electrolyte interphases. *Nano Lett.* **14**, 1405–1412 (2014).

13. Kim, H., Kim, M. G., Jeong, H. Y., Nam, H. & Cho, J. A new coating method for alleviating surface degradation of $LiNi_{0.6}Co_{0.2}Mn_{0.2}O_2$ cathode material: nanoscale surface treatment of primary particles. *Nano Lett.* **15**, 2111–2119 (2015).

14. Luo, J., Cheng, H. K., Asl, K. M., Kiely, C. J. & Harmer, M. P. The role of a bilayer interfacial phase on liquid metal embrittlement. *Science* **333**, 1730–1733 (2011).

15. Cho, J., Wang, C. M., Chan, H. M., Rickman, J. M. & Harmer, M. P. Role of segregating dopants on the improved creep resistance of aluminum oxide. *Acta Mater.* **47**, 4197–4207 (1999).

16. Buban, J. P. et al. Grain boundary strengthening in alumina by rare earth impurities. *Science* **311**, 212–215 (2006).

17. Shibata, N. et al. Observation of rare-earth segregation in silicon nitride ceramics at subnanometre dimensions. *Nature* **428**, 730–733 (2004).

18. Appapillai, A. T., Mansour, A. N., Cho, J. & Shao-Horn, Y. Microstructure of $LiCoO_2$ with and without 'AlPO_4' nanoparticle coating: combined STEM and XPS studies. *Chem. Mater.* **19**, 5748–5757 (2007).

19. Lee, Y. et al. Facile formation of a Li_3PO_4 coating layer during the synthesis of a lithium-rich layered oxide for high-capacity lithium-ion batteries. *J. Power Sources* **315**, 284–293 (2016).

20. Sun, K. & Dillon, S. J. A mechanism for the improved rate capability of cathodes by lithium phosphate surficial films. *Electrochem. Commun.* **13**, 200–202 (2011).

21. Li, X. et al. Atomic layer deposition of solid-state electrolyte coated cathode materials with superior high-voltage cycling behavior for lithium ion battery application. *Energy Environ. Sci.* **7**, 768–778 (2014).

22. Miller, D. J., Proff, C., Wen, J. G., Abraham, D. P. & Bareño, J. Observation of microstructural evolution in Li battery cathode oxide particles by in situ electron microscopy. *Adv. Energy Mater.* **3**, 1098–1103 (2013).

23. Bak, S.-M. et al. Structural changes and thermal stability of charged $LiNi_xMn_yCo_zO_2$ cathode materials studied by combined in situ time-resolved XRD and mass spectroscopy. *ACS Appl. Mater. Interfaces* **6**, 22594–22601 (2014).

24. Lim, J.-M. et al. Intrinsic origins of crack generation in Ni-rich $LiNi_{0.8}Co_{0.1}Mn_{0.1}O_2$ layered oxide cathode material. *Sci. Rep.* **7**, 39669 (2017).

25. Wang, H., Jang, Y. I., Huang, B., Sadoway, D. R. & Chiang, Y. M. TEM study of electrochemical cycling-induced damage and disorder in $LiCoO_2$ cathodes for rechargeable lithium batteries. *J. Electrochem. Soc.* **146**, 473–480 (1999).

26. Kim, J. et al. Controllable solid electrolyte interphase in nickel-rich cathodes by an electrochemical rearrangement for stable lithium-ion batteries. *Adv. Mater.* **30**, 1704309 (2018).

27. Ryu, H.-H., Park, K.-J., Yoon, C. S. & Sun, Y.-K. Capacity fading of Ni-rich $Li[Ni_xCo_yMn_{1-x-y}]O_2$ ($0.6 \leq x \leq 0.95$) cathodes for high-energy-density lithium-ion batteries: bulk or surface degradation? *Chem. Mater.* **30**, 1155–1163 (2018).

28. Yan, P. et al. Intragranular cracking as a critical barrier for high-voltage usage of layer-structured cathode for lithium-ion batteries. *Nat. Commun.* **8**, 14101 (2017).

Author contributions

C.W., J.Z. and J-G.Z. initiated this research project. J.Z. and J.L. synthesized the cathode materials. J.L., B.W., X.C., Y.Z. and X.S. carried out the ALD coating. J.Z. and X.C. performed battery tests. P.Y. conducted the TEM and SEM analyses. P.Y., J.Z., C.W. and J.-G.Z. prepared the manuscript with the input from all the other co-authors.

Competing interests

The authors declare no competing interests.

Additional information

Supplementary information is available for this paper at https://doi.org/10.1038/s41560-018-0191-3.

Reprints and permissions information is available at www.nature.com/reprints.

Correspondence and requests for materials should be addressed to X.S. or C.W. or J.-G.Z.

Publisher's note: Springer Nature remains neutral with regard to jurisdictional claims in published maps and institutional affiliations.